CrossMark

An Improved Method to Measure Head Echoes Using a Meteor Radar

Peter A. Panka[1] , Robert J. Weryk[2] , Juan S. Bruzzone[1,3] , Diego Janches[1] , Carsten Schult[4], Gunter Stober[5] , and Jose Luis Hormaechea[6,7]

[1] ITM Physics Laboratory, NASA Goddard Space Flight Center, Code 675, 8800 Greenbelt Road, Greenbelt, MD 20771, USA; panka.alex@gmail.com
[2] Institute for Astronomy, University of Hawaii, 2680 Woodlawn Drive, Honolulu, HI 96822, USA
[3] Department of Physics, Catholic University of America, 620 Michigan Avenue NE, Washington, DC 20064, USA
[4] Leibniz Institute of Atmospheric Physics at the Rostock University, Schloss-Str. 6, 18225 Kühlungsborn, Germany
[5] Institute of Applied Physics, Microwave Physics, University of Bern, Bern, Switzerland
[6] Facultad de Ciencias Astronómicas y Geofísicas, Universidad Nacional de La Plata, La Plata, Argentina
[7] Estación Astronómica Rio Grande, Rio Grande, Tierra del Fuego, Argentina
Received 2021 January 22; revised 2021 August 18; accepted 2021 August 22; published 2021 September 20

Abstract

We present an improved methodology to obtain absolute position and velocity of meteor head echoes, which can yield orbital information, generally limited to the use of High-Power, Large-Aperture radars, using an advanced-designed specular meteor radar. The observations, which were performed during a period when an outburst of the β-Taurid meteor shower was expected, were performed with the Southern Argentine Agile MEteor Radar. Three different methodologies are utilized to confirm our results: an improved interferometric solver building on previous work, and two different target localization techniques using remote receiving stations. In addition, we performed simultaneous optical observations during the meteor shower period. Overall, 71 radar head echo events were detected and analyzed using interferometry, while 12 of those events have detected signals strong enough to be analyzed using localization methods at the remote sites. Due to poor weather, however, the optical cameras only observed two events simultaneously with the radar. Results from these events are in agreement with the radar results. We find that interferometry methods from both radar and optical data resulted in the most accurate estimation of meteor properties, while target localization techniques derived similar results, albeit with larger uncertainty. We also computed heliocentric meteoroid orbits, and while a fraction was hyperbolic, we believe these to be due to uncertainty. Two events are suspected to be β-Taurid shower members.

Unified Astronomy Thesaurus concepts: Radio interferometry (1346); Meteor showers (1034); Radar telescopes (1330)

1. Introduction

As a meteoroid with mass 1–1000 μg enters Earth's atmosphere, it does so at speeds between 11 and 72 km s^{-1}, having enough kinetic energy loss to ablate and subsequently ionize the surrounding neutral atmosphere. This process typically occurs between 70 and 140 km (Vondrak et al. 2008; Janches et al. 2017), and the ionized plasma, traveling at similar speed to the meteoroid, can be observed using ground-based radar facilities. Radars observe the reflection of the transmitted radio signals scattered off the surrounding dense plasma regions, otherwise known as a meteor head echo. This radar target has a much smaller cross section than the more commonly observed meteor trail echo (Baggaley 2002; Kero et al. 2019; Schult et al. 2021), requiring specific High-Power, Large-Aperture (HPLA) radar facilities that transmit peak pulse power ranging from 1 to 6 MW through very narrow beam widths (0.08°–3.6°; Janches et al. 2014a). Meteor head echo measurements provide information on the evolution of the meteor as a function of time, thus allowing us to constrain the characteristics of the incoming meteoroid flux, and in particular the physical processes occurring during ablation and ionization (Mathews et al. 2001; Close et al. 2005, 2012; Dyrud & Janches 2008; Fentzke & Janches 2008; Janches et al. 2009, 2014b; Stober et al. 2013). HPLA radars can efficiently detect and quantify a large number of meteor head echoes, specifically the more

abundant, lower end of the incoming mass distribution due to the high power density resulting from high-power transmission and a narrow beam (Janches et al. 2014a). In theory, meteors produced by particles with larger masses can also be observed by HPLA radars, but the probability that these meteors pass through the narrow radar beam decreases with increasing size (Janches et al. 2017). For those HPLA radar systems that have interferometric or multi-receiving-configuration head echo observations can be utilized to determine the precise knowledge of a meteor location and its absolute trajectory and velocity. This, in turn, provides a venue to derive the meteor's radiant and orbit. The list of such instruments is very short: the Jicamarca Radio Observatory (JRO; Chau & Woodman 2004), the Advanced Research Projects Agency Long-Range Tracking and Instrumentation Radar (ALTAIR; Close et al. 2000, 2002), the Middle and Upper (MU) Atmosphere (Kero et al. 2011, 2012; Pifko et al. 2013), the Poker Flat Incoherent Scatter Radar (PFISR; Sparks et al. 2010), and the Middle Atmosphere Alomar Radar System (MAARSY; Schult et al. 2013, 2017). In addition, the European Incoherent SCATter radar system (EISCAT) can also determine meteor positions and absolute velocities using common volume observations utilizing multiple remote receiving sites (Kero et al. 2008b). The EISCAT 900 MHz radar has a single transmitter and receiver at their central station in Tromsø, Norway, as well as a single receiver at each of two separate remote sites over 200 km away, in Kiruna, Sweden, and Sodankylä, Finland. The meteor's location is determined as the intersection point of three geometrical shapes centered around the three isolated radar sites, otherwise known as target localization (Kero et al. 2008b). The 430 MHz Arecibo Observatory (AO),
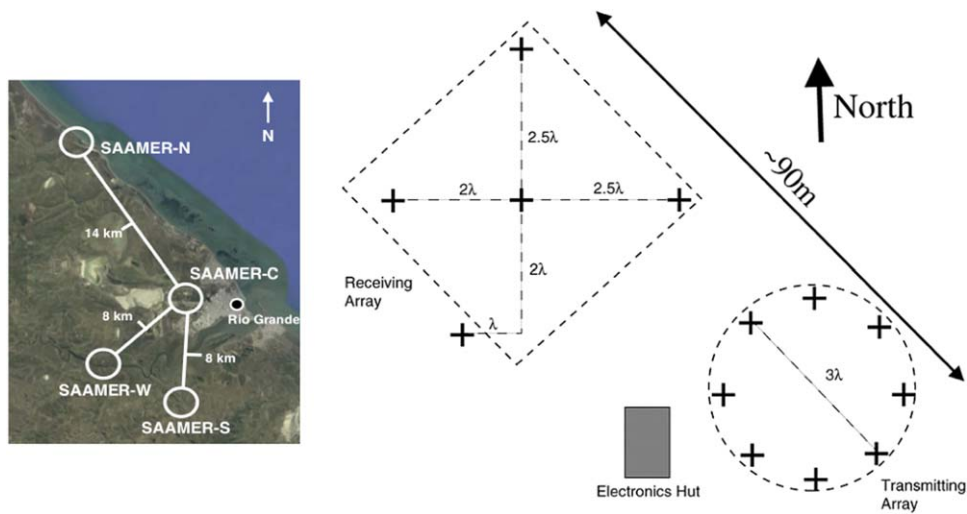
Figure 1. Left: SAAMER-OS geographic layout (© Google Maps 2020). Right: antenna transmitter and receiver layout at SAAMER-C in Rio Grande, Tierra del Fuego.

which was the most sensitive HPLA radar, had the narrowest beam and thus was sensitive to the smallest meteoroids (Janches et al. 2014b, 2015b, 2017). While it could measure line-of-sight (LOS) Doppler velocities with high precision, it was not capable of determining 3D meteor trajectories as a result of having only a single receiver (Janches et al. 2000b).

Only recently have non-HPLA radars developed the capabilities of detecting meteor head echoes (Schult et al. 2015; Marshall et al. 2017). Janches et al. (2014a) demonstrated that lower-power all-sky Very High Frequency (VHF) meteor radars with advanced designs such as the Southern Argentina Agile MEteor Radar (SAAMER) can also be used to detect such events. SAAMER transmits significantly less power (64 kW) compared to HPLA systems but 510 times more power than standard all-sky VHF meteor radars. In this work, we build on the work first reported by Janches et al. (2014a) to improve the meteor head echo interferometric observing technique, and we use a more suitable pulse scheme for a low-power VHF system. In addition, we make use of the full SAAMER Orbital System (hereafter referred to as SAAMER-OS; Janches et al. 2015a, 2020), which consists of four additional remote receiving stations, spaced 5–13 km from the central transmitting station, to detect the forward scatter from each meteor head echo. This allows for multiple approaches to determine meteor head echo velocity and directions and thus validate the derived results. Finally, we also performed simultaneous observations using optical video cameras of meteor head echoes detected by SAAMER-OS, similarly done by Michell et al. (2015). The structure of the paper is as follows: Section 2 discusses in detail the system characteristics, while Section 3 describes our data analysis methodology and various approaches to derive the meteor location. In Section 4, we present a summary and discussion of the most representative results and distributions from the head echo observations utilizing SAAMER-OS, and we give final remarks in Section 5.

2. Experiment Overview

We performed radar and optical observations during a period of expected activity of the β-Taurid meteor shower, between

2019 June 26 and 30. An overview of the radar and optical hardware and operation is presented in the following sections.

2.1. SAAMER-OS

SAAMER-OS is hosted by the Estacion Astronómica Rio Grande (EARG) in the city of Rio Grande, Tierra del Fuego, Argentina. At the time of our observations, it consisted of four stations (see Figure 1): the central station (SAAMER-C; 53.786S°, 67.751°W), where the transmitting and interferometry-enabled receiving antennas are located; the northern remote station (SAAMER-N; 53.682°S, 67.871°W), located 14 km northwest of the central station; the western remote station (SAAMER-W; 53.828°S, 67.842°W), located 8 km southwest of the central station; and the southern remote station (SAAMER-S; 53.852°S, 67.759°W), located 8 km directly south of the central station. Currently, there is a fifth station (SAAMER-E; 53.772°S, 67.727°W), which was not used in this study since it was deployed in 2019 September, located 4 km northeast of the SAAMER-C. Each remote site has a single three-element crossed yagi receiving antenna identical to those forming the interferometer array at SAAMER-C.

The transmitting phased array utilized for this study consists of eight three-element crossed yagi antennas arranged in a circle of 27.6 m (three wavelengths) diameter. The plasma surrounding the meteoroid, otherwise known as the head echo, has a small radar cross section requiring high detection sensitivity and temporal resolution. Therefore, as similarly done by Janches et al. (2014a; see Figure 2 in that work), all antennas transmitted in phase, resulting in most of the radiated power directed upward in a relatively narrow beam with a 3 dB decrease in power at ∼8° off zenith at ∼100 km altitude.

Specifically to the campaign reported in this paper, a series of upgrades were made in comparison to the initial campaign reported by Janches et al. (2014a), to improve our estimates of meteoroid velocities and orbits. Table 1 displays a summary of SAAMER-OS's operating characteristics utilized during this observing campaign. First, we modified the transmitting mode employing a 22.5 μs long 7 bit Barker code and a pulse repetition frequency (PRF) of 950 Hz, resulting in an effective interpulse period (IPP) of 1.1 ms. The sampling range resolution of all receivers was 500 m. For reference, Janches et al. (2014a) used a

Figure 2. Location of ONAS-DREAM stations in relation to the SAAMER-OS configuration (© Google Maps 2020).

Table 1
SAAMER's Operating Characteristics for Head Echo Mode

Quantity	SAAMER-OS
Latitude	53.8°S
Longitude	67°W
Frequency	32.55 MHz
PRF	950 Hz
Peak transmitted power	64 kW
Bandwidth	125 kHz
Coherent integrations	1
Barker code	1110010
Pulse length	22.5 μs
Sampling resolution	500 m
FWHM	8°

13.6 μs long monopulse, a sampling resolution of 250 m, and poorer temporal resolution with an IPP of 2 ms applying an additional coherent integration, resulting in an effective IPP of 4 ms. Utilization of pulse coding enables the use of longer pulses and thus more transmitted energy, while at the same time being able to maintain range resolution. Furthermore, applying deconvolution techniques to decode the returned signal provides an additional increase in signal-to-noise ratio (S/N). In our case, the S/N improvement due to the decoding is approximately 16.9 dB (with a 7 bit Barker compared to a monopulse).

At SAAMER-C, the central antenna of the receiving array is located 90 m from the center of the transmitting array (Figure 1) and is configured by a modified version of the typical five-antenna interferometer arrangement used in meteor radars (Jones et al. 1998; Hocking et al. 2001). As in Janches et al. (2014a), we used interferometry to determine the 3D meteor head echo path and thus the absolute velocity. In this work we also improve our observing and data analysis scheme by (1) the determination of LOS Doppler velocities via pulse-to-pulse cross-correlation calculations (Janches et al. 2000a) and (2) the use of the remote sites to perform multistatic observations of the same event in order to obtain absolute velocities via triangulation methods. The details of these techniques are provided in Section 3.

2.2. ONAS-DREAM

In addition to radar measurements, we deployed video cameras to perform simultaneous optical and radar observations of the same head echo event. The Optical Network At SAAMER for the Detection of Radar Echoes Arising from Meteors (ONAS-DREAM) began operations in late 2018 December and has three stations to record video meteors observed simultaneously with SAAMER-OS. The first station is colocated with the SAAMER-S remote station, the second is colocated with SAAMER-E, and the third station is located near 53.952°S, 68.265°W, roughly 38.3 km SW of SAAMER-C. Figure 2 displays the configuration of the ONAS-DREAM network with respect to SAAMER-OS. Each station hosts an indoor computer for controlling image acquisition and data reduction, as well as a single narrow-field low-light Watec WAT902H2 Ultimate camera within a weather-sealed security camera enclosure. The computer clocks are synced to dedicated Internet Time Servers using the Simple Network Time Protocol. To increase the likelihood of detecting simultaneous video meteors, the cameras are aimed at a volume of sky 110 km above SAAMER-C. The reference height of 110 km was chosen as that is where most head echoes are observed by SAAMER during the initial experiment (Janches et al. 2014a). Figure 3 showed the regions where the cameras' field of view (FOV) and the radar beam overlap at four different altitudes. The cameras record interlaced video at 30 frames per second at 640 × 480 pixel resolution, and each camera is affixed with a Navitar 17 mm f/0.95 lens, resulting in 15.9° × 21.4° FOV at 2′ pixel^{-1}. The cameras have a limiting stellar magnitude of +5.4 and detect meteors between magnitude +4 and −5, which typically correspond down to sub-centimeter-size meteoroids. As argued by Janches et al. (2014a), SAAMER-detected meteor head echoes are most likely produced by particles in this size range, given its lower sensitivity with respect to HPLA radars commonly used to detect these targets. Initial optical–radar comparison of SAAMER-detected head echoes performed by Michell et al. (2015) utilizing a more sensitive Andor Ixon DU-888 EMCCD imager estimated masses
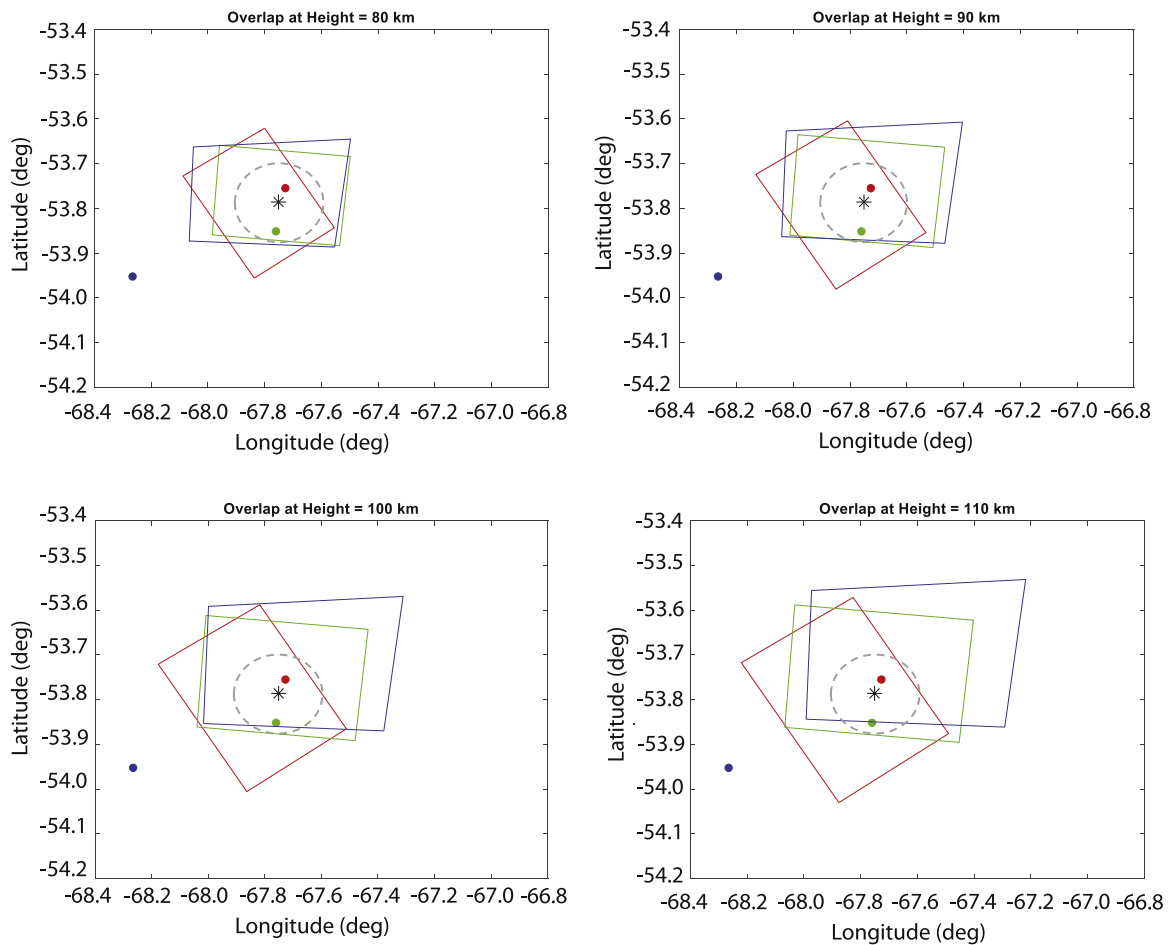
Figure 3. FOV of the ONAS-DREAM stations, represented as color rectangles, at different altitude. The red, blue, and green circles show the location of each optical station. The gray dotted circle represents the region in the sky where the transmitted power is at higher than 3 dB from the peak. The star at the center is the location of SAAMER-C.

between ∼0.3 and 1.5 mg for six simultaneously detected meteor head echo events.

Meteor detection and meteoroid orbit determination are achieved with the MeteorScan software suite (Gural [1995], [1997], [2012]), including a meteor deceleration correction based on Whipple & Jacchia ([1957]) and Jacchia & Whipple ([1961]) as part of the reduction pipeline. We refer the reader to Jenniskens et al. ([2011]) for a detailed description of optical meteor data reduction steps.

3. Meteor Radar Data Analysis

The methodology used during this study first scans the raw radar data using a sliding time window in the power domain (Figure [4]) and searches for signals that are at least 3σ above the background noise. The background noise is determined by taking the median signal value within each Range–Time–Intensity (RTI) image spanning 180 range gates and 2000 IPPs. This significantly reduces the volume of raw data to be processed; however, it does not isolate the head echoes from trail echoes and noise triggers. Because head echoes move at hypersonic speeds on the order of tens of kilometers per second, the leading edge of the echo will span several range gates and be detected for periods generally shorter than a second (Janches et al. [2000a], [2014a]; Sparks et al. [2009]; Kero et al. [2011]; Stober et al. [2013]; Schult et al. [2017]). In comparison, specular meteor trail echoes, which move at m s^{-1} speed drifted by the mesospheric background wind, will be
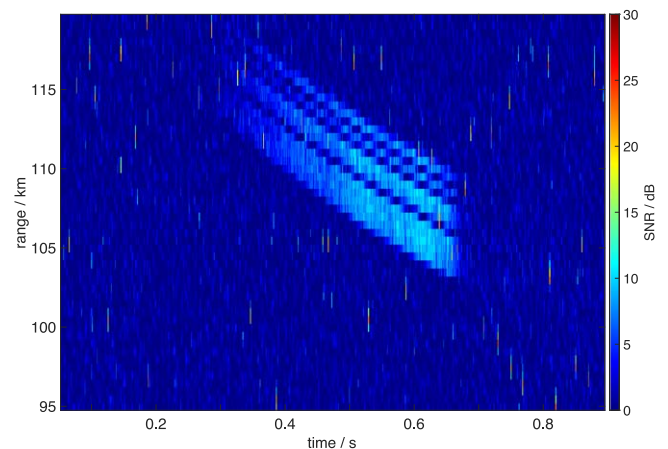

Figure 4. RTI image from SAAMER-C of an undecoded raw head echo event. No noise filter applied.

detected over longer periods of time with negligible shift in range as a function of time (McKinley [1961]; Mazur et al. [2020]; Schult et al. [2020]). Figure [5] shows a weak and strong head echo followed by the trail echo observed at SAAMER-C. It can be observed for the strong event (bottom panels) in this figure that the leading edge of the head echo spans several range gates, equivalent to ∼2.5 km in range in about ∼0.3 s. The subsequent
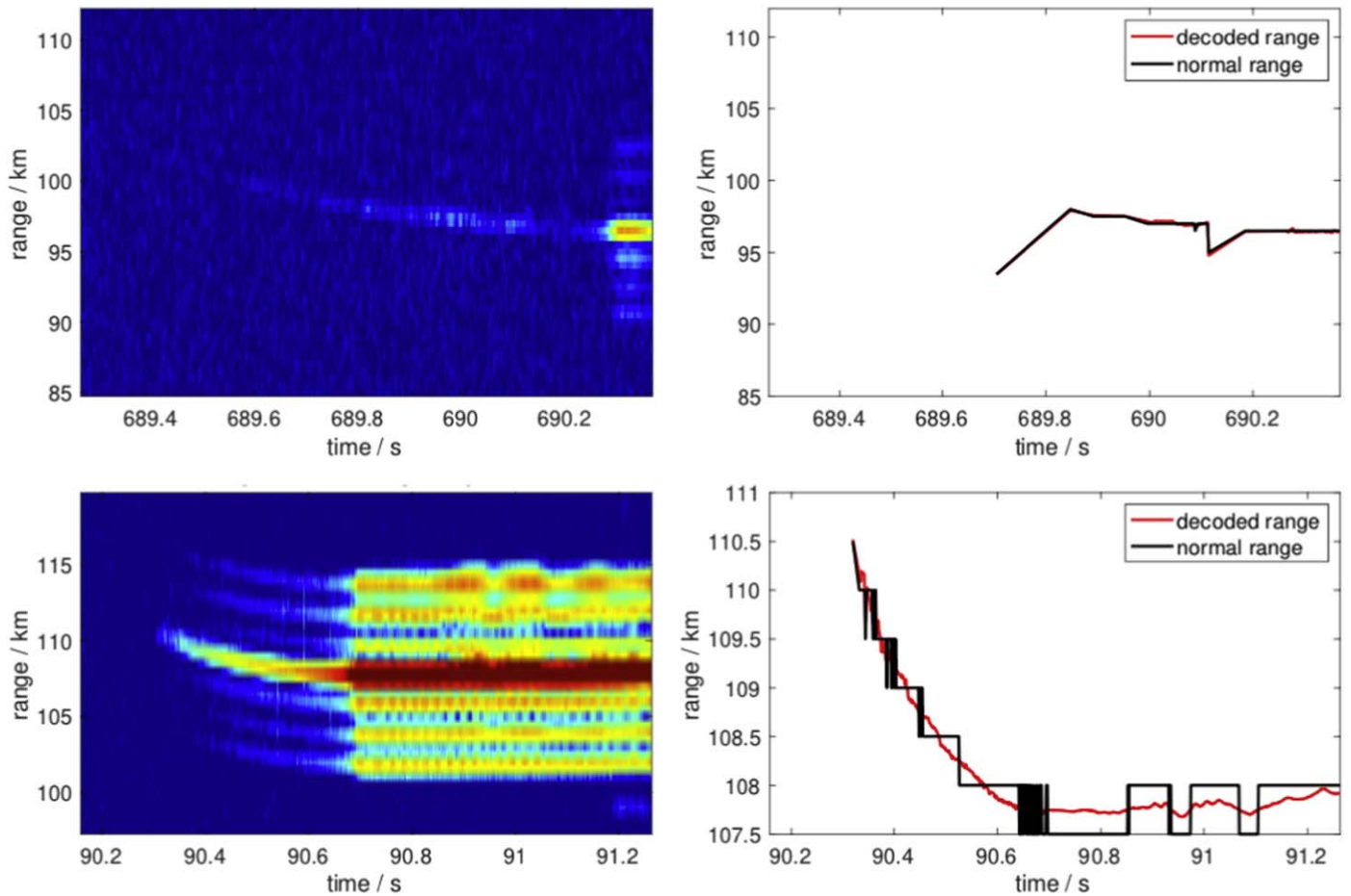
Figure 5. Left: RTI image from SAAMER-C of a weak (top) and strong (bottom) head echo event followed by the meteor trail echo. Right: normal (black) and decoded (red) ranges derived from the head echo.
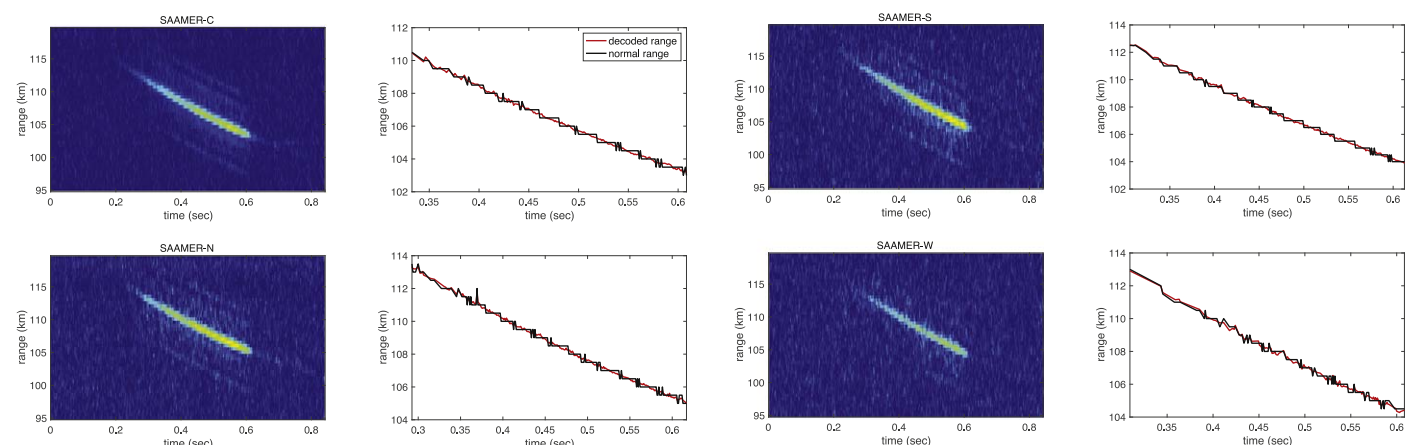

Figure 6. RTI images from SAAMER-C, SAAMER-N, SAAMER-S, and SAAMER-W and respective normal (black) and decoded (red) ranges derived from their corresponding head echoes.

trail echo, on the other hand, has a leading edge confined to one range gate for at least the remaining 0.7 s display in the figure. This particular event has such high S/N that even after pulse decoding the resulting sidelobes due to the use of a barker code are still present in the RTI plot. Although the weak event (top panels) is visible in this figure, only a few data points had a large enough S/N to extract range data. Since the top right panel shows sparse decoded and normal range profiles, extracting any position

and velocity information about the head echo event would be very challenging and likely result in large uncertainties. A handful of these weak events were observed during the campaign; however, due to the weak S/N, these events were not included in the 71 events we analyzed.

Figure 6 shows an example of a head echo without the presence of a trail echo that was detected at all stations. This event is the same event as the one displayed in Figure 4. A

noise filter and decoding algorithm have been applied to the data presented in Figure 6. The colored images in the first and third columns are RTI plots for each station. For SAAMER-C, the event was detected in six different channels (five interferometer antennas plus the transmitting array used as an additional receiver; see Janches et al. 2014a, for details). The top left panel of Figure 6 is the average power from those six channels, ultimately resulting in a higher S/N in comparison with the signals from SAAMER-N, SAAMER-S, and SAA-MER-W single receivers. The panels in the second and fourth columns of Figure 6 show both the undecoded and decoded range versus time calculations. The undecoded range profiles (black) follow a discrete path along the range gates separated by the sampling resolution of 500 m. The decoded range (red) is determined using a Doppler-shifted pulse-coding algorithm, which uses the degree of asymmetry of the decoded signal to interpolate the code used in the decoding procedure to improve the S/N threshold and the range resolution from the over-sampled 7 bit Barker code. This algorithm can localize the target to within a few hundredths of a range gate and is described in detail by Kero et al. (2008a).

The position of a head echo observed by SAAMER can be determined in several ways. The first method, used by Janches et al. (2014a), leverages the five-antenna interferometer arrangement at SAAMER-C (Figure 1) to determine the spatial location from each pulse applying commonly used interfero-metric techniques, i.e., phase-difference estimations between receiving antenna pairs. In particular, in this work we follow the formulation described in Hocking et al. (1997, 2001) and Lau et al. (2006) to determine the meteor position. It is important to note that using a 7 bit Barker code improves the accuracy of the range estimation and ultimately the head echo absolute position in comparison with those determined by Janches et al. (2014a) using a monopulse. For the case of a five-receiver interferometry, the following formulation is used:

$$
\begin{bmatrix} \phi_{01} \\ \phi_{02} \\ \phi_{03} \\ \phi_{04} \end{bmatrix} = \begin{bmatrix} -\dfrac{2\pi}{\lambda}d_{01}\cos(\gamma_{01}) & -\dfrac{2\pi}{\lambda}d_{01}\sin(\gamma_{01}) \\ -\dfrac{2\pi}{\lambda}d_{02}\cos(\gamma_{02}) & -\dfrac{2\pi}{\lambda}d_{02}\sin(\gamma_{02}) \\ -\dfrac{2\pi}{\lambda}d_{03}\cos(\gamma_{03}) & -\dfrac{2\pi}{\lambda}d_{03}\sin(\gamma_{03}) \\ -\dfrac{2\pi}{\lambda}d_{04}\cos(\gamma_{04}) & -\dfrac{2\pi}{\lambda}d_{04}\sin(\gamma_{04}) \end{bmatrix}
$$
$$
\cdot \begin{bmatrix} \cos(\theta)\cos(\varphi) \\ \cos(\theta)\sin(\varphi) \end{bmatrix}, \tag{1}
$$

where ϕ_{ij} represents the phase difference between receiver pair (j, i). For this analysis, we considered only differences with the central receiver (#0). The relative positions of each antenna are represented as d_{0k} and γ_{0k}, which define the distance and angle between each receiver pair, respectively. The radar wavelength is given by $\lambda = 9.2$ m, and θ and φ are the zenith and azimuth angles of each IPP received signal, respectively. Equation (1) can be written as

$$
b = Ax, \tag{2}
$$

where b is the vector containing the phase differences, A is a matrix containing the distances and angles between correlated

receivers, and x is a vector that contains information about the angle of arrival (AOA) of the scattered pulse.

The least-squares solution of Equation (2) is

$$
x = \begin{bmatrix} \cos(\theta)\cos(\varphi) \\ \cos(\theta)\sin(\varphi) \end{bmatrix} = \begin{bmatrix} x_1 \\ x_2 \end{bmatrix} = (A^T A)^{-1} A^T b. \tag{3}
$$

The AOA can be estimated using

$$
\theta = \sin^{-1}(\sqrt{x_1^2 + x_2^2}), \ \varphi = \tan^{-1}\left(\frac{x_2}{x_1}\right). \tag{4}
$$

To account for any ambiguity present owing to phase aliasing, we iterate all phase differences ϕ_{0k} by shifting them by $2\pi n$, where n ranges from ± 0 to 5. We then substitute the new zenith θ and azimuth φ estimate into Equation (1) and calculate phase residuals. The zenith and azimuth angles that minimize the phase residuals are taken to be the best-fit solution to the AOA. From the zenith and azimuth angles and measured range, trigonometry relations are applied to calculate the position of the meteor in Cartesian coordinates.

The second method to determine the meteor position is similar to the one used by Kero et al. (2008a) for tristatic observations with the 930 MHz EISCAT system. This methodology requires simultaneous observations from at least three radar stations, and the work reported here represents the first time ever utilized by a non-HPLA meteor radar (or any other radar besides the EISCAT 930 MHz system). The true meteor position is situated at the intersection of three geometrical shapes: a sphere centered at SAAMER-C and two prolate spheroidal surfaces, both with SAAMER-C at one focal point and a remote station at the other (see right panel of Figure 7). The formulation to solve for the meteor position is

$$
x^2 + y^2 + z^2 = r_c^2 \tag{5}
$$

$$
(x - x_i)^2 + \frac{(y - y_i)^2}{a_i^2} + \frac{(z - z_i)^2}{b_i^2} = 1 \tag{6}
$$

$$
(x - x_{i+1})^2 + \frac{(y - y_{i+1})^2}{a_{i+1}^2} + \frac{(z - z_{i+1})^2}{b_{i+1}^2} = 1, \tag{7}
$$

where the radius of the sphere centered at SAAMER-C is equal to its respective decoded range, r_c in Equation (5). The prolate spheroidal surfaces for the remote sites are defined in Equations (6) and (7), where x_i, y_i, z_i and x_{i+1}, y_{i+1}, z_{i+1} are the positions of the remote radar stations in Cartesian coordinates and a and b are the semimajor and semiminor axes, respectively. The total range from SAAMER-C to the meteor to a remote receiver is equal to $2a$ and can be calculated by multiplying the decoded range from the forward-scattered measurements by 2. The semiminor axis, b, can be calculated from the expression $b^2 = a^2 - c^2$, where c is half the distance from SAAMER-C to the remote site. The position of the meteor is determined by finding the x, y, and z values that simultaneously solve Equations (5)–(7).

The third method is very similar to the second, but instead of using prolate spheroidal surfaces for the remote sites, we simply use spheres identical to Equation (5). For this method, the position of the meteor is determined by finding the x, y, and z values that simultaneously solve the spherical equations at all radar stations as follows (see left panel of Figure 7):
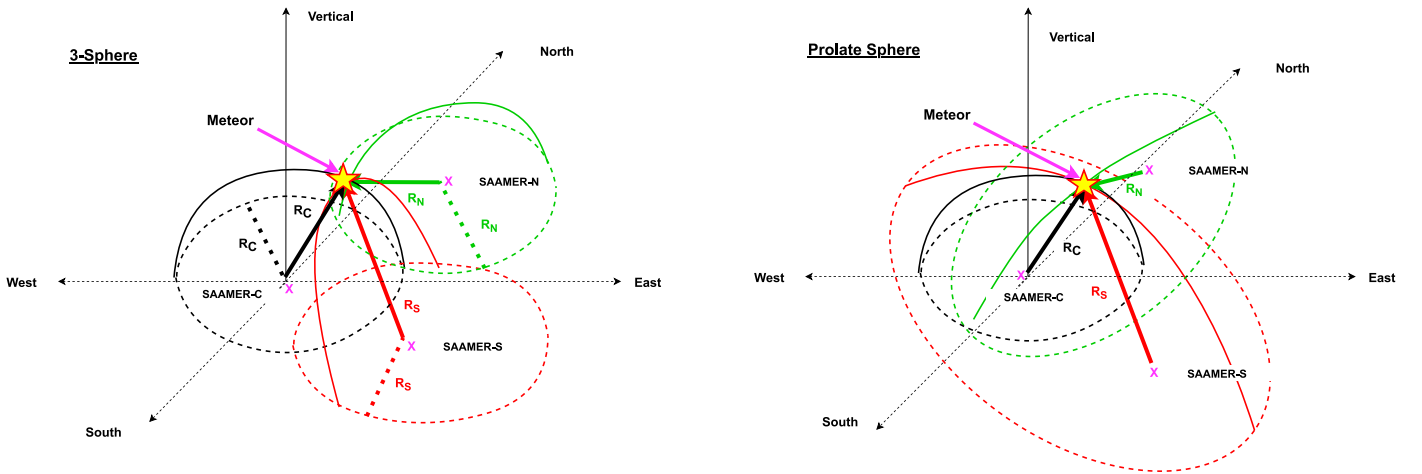
$$
x^2 + y^2 + z^2 = r_c^2 \tag{8}
$$

Figure 7. Top-view schematic of the 3-sphere and prolate sphere geometries for determining meteor location from the forward-scattering process. Solid lines represent the cross section of the three-dimensional geometrical shapes with Earth's surface. Dotted lines represent ranges projected on the surface.
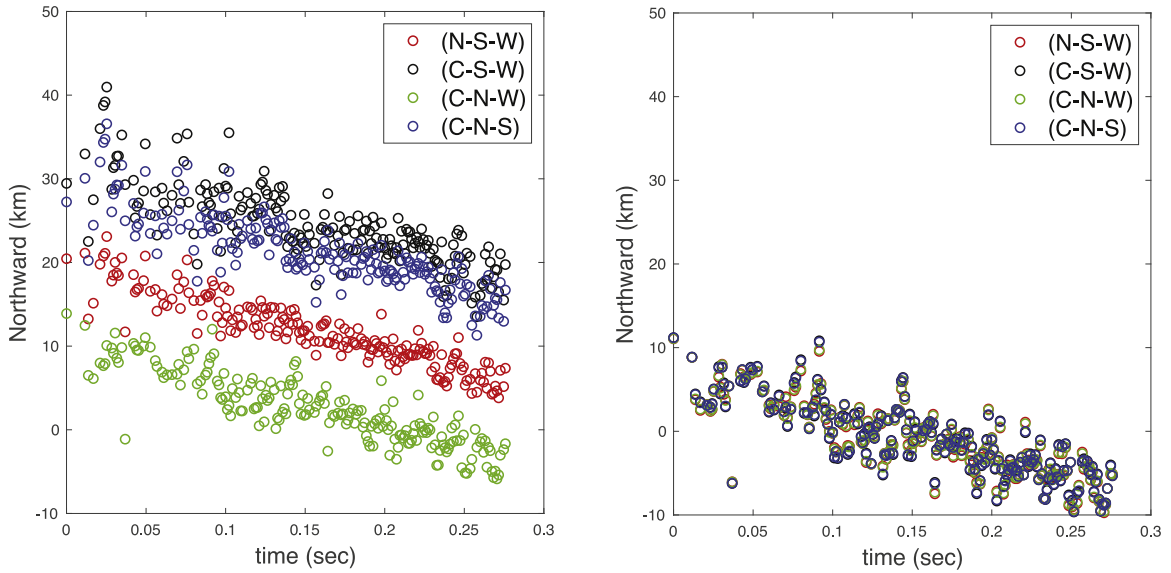

Figure 8. Derived northward position vectors using uncorrected (left) and corrected (right) SAAMER-C ranges for four combinations of radar stations (red: North–South–West; black: Central–South–West; green: Central–North–West; blue: Central–North–South). Same event as in Figure 6.

$$(x - x_i)^2 + (y - y_i)^2 + (z - z_i)^2 = r_i^2 \qquad (9)$$

$$(x - x_{i+1})^2 + (y - y_{i+1})^2 + (z - z_{i+1})^2 = r_{i+1}^2, \qquad (10)$$

where r_c, r_i, and r_{i+1} are the decoded ranges at the central and remote sites, respectively. The solutions to these equations are also found analytically.

All three methods rely on an accurate estimation of the range calculated with respect to each radar receiving station. The range estimation at SAAMER-C influences the interferometry solution only slightly, as this method mostly relies on phase differences between antenna pairs in the five-receiver antenna array. The solutions to the prolate sphere and 3-sphere method, however, are significantly more sensitive to the decoded ranges, as Equations (5)–(10) are dependent on these variables. If the decoded ranges are not corrected by small offsets, then all three methods will result in different meteor positions at each pulse. Finding the solution to these small offsets can be optimized if at least four radar stations are observing the same target. This is shown in the left panel of Figure 8, where the

results using a different combination of receiving stations are shown to exhibit significant differences. In particular in this panel, which is the same event discussed in Figure 6, we show the results in the northward component for the 3-sphere method using the following combinations: North–South–West (N–S–W), Central–South–West (C–S–W), Central–North–West (C–N–W), and Central–North–South (C–N–S), resulting in differences exceeding 20 km, although the general slopes of the trajectories are similar. The westward and vertical components of the derived meteor head echo position (not displayed in the figure) also show similar offsets. To correct for these differences and converge to a unique solution, we only need to vary the SAAMER-C range. Because there is no transmitter colocated at the remote sites, the decoded ranges for them are equal to the range of the transmitted signal from SAAMER-C to the meteor added to the range from the meteor to the respective remote site and then divided by 2, which we call the bisector range: $(R_{\text{bisector}} = (R_{\text{remote}} + R_{\text{saamer-c}})/2)$. Therefore, the remote ranges are directly dependent on the range at SAAMER-C.
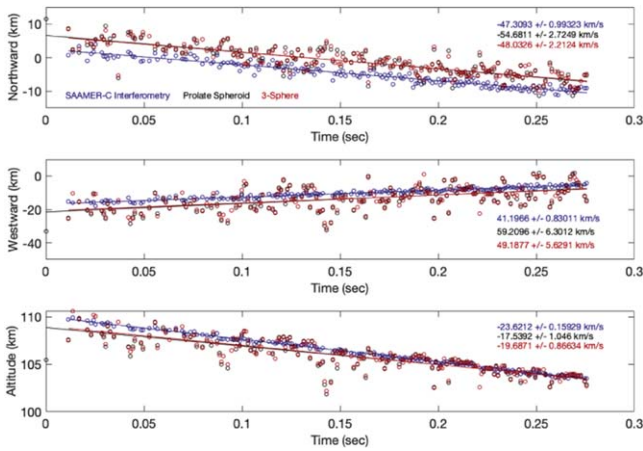
Figure 9. Derived position trajectories using SAAMER-C interferometric capabilities (blue), Prolate sphere method (black), and the 3-sphere method (red). Respective velocities and their uncertainties are displayed. Same event as in Figure 3.

Figure 10. Illustration of the forward scatter from SAAMER-C to SAAMER-S for two radar pulses. The ranges, bisector vector, and angle between the bisector vector and the meteor trajectory are displayed.

To solve this discrepancy, we developed a numerical approach where the range at SAAMER-C is adjusted by 100 m increments and the 3-sphere problem is solved for each combination of radar stations at each increment. We assume that the true range is the one that results in the same meteor position for all combinations of receiving stations. This is shown in the right panel of Figure 8, where the resulting northward trajectory for each radar site combination is displayed after the ranges have been corrected. For this particular case the range at SAAMER-C was decreased by ∼200 m, while the respective remote ranges were increased by the same amount. Applying the same methodology to all the observed events, we find that the derived offset is different for each head echo event, ranging between 100 and 800 m, and thus exceeding in some cases the 500 m sampling range resolution. We also find that deriving the position and velocity vectors using the prolate sphere and 3-sphere approach is most accurate when range estimates are known to within 200 m at each pulse. Otherwise, the solution will have uncertainties as large as 20 km, similar to the ones displayed in the left panel of Figure 8. Due to the small number of high-S/N events that were simultaneously observed at all four stations, a relationship between range offsets and meteor parameters could not be determined with confidence. We will investigate these offsets in a future study.

The results using the three methods described above are compared in Figure 9. The vertical, northward, and westward components of the meteoroid trajectories are plotted, as well as the respective velocities with errors derived from the slope of a linear fit to the individual position estimates. The ranges have been corrected, and all three methods derive similar trajectory trends, validating these approaches. The vector velocities are also similar to one another within their uncertainties. The interferometric results at SAAMER-C have the lowest uncertainties, while using the remote site for the other two methods shows slightly higher velocity error. Overall, all three methods used to calculate the meteor trajectory produce similar results. In Section 4.1 we will also use simultaneous video observations as an independent method to verify our results.

Finally, in addition to estimating meteoroid speed by performing a linear fit to the derived position as a function of time, velocities can be calculated from the Doppler signatures for individual pulses received at each radar station. The LOS Doppler meteor velocity is determined from the pulse-to-pulse
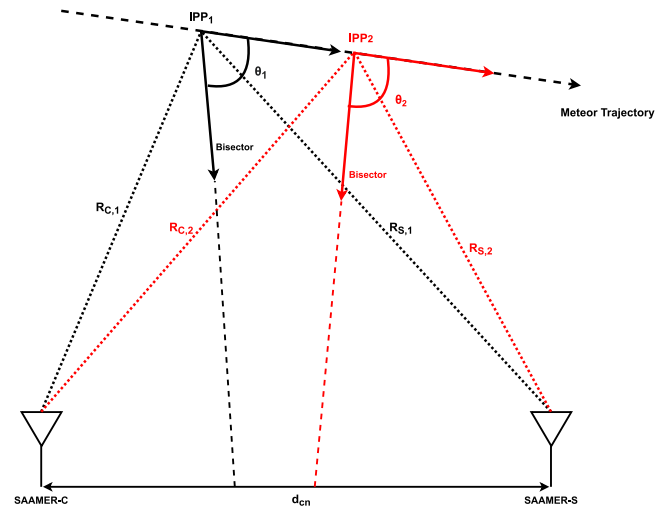
correlation function and pulse-to-pulse Doppler phase shift (Hagen & Farley 1973; Mathews 1976). An example application of this for head echo measurement is given by Janches et al. (2000a). The former utilizes the in-phase and in-quadrature components of the returned signal and their pulse separation. The latter requires solving for the ambiguity velocity due to the 2π phase aliasing, which for the given radar wavelength and pulse separation is 4.37 km s^{-1}. Then, the average meteor velocity given by the range-rate trajectory is needed as a reference point to solve this ambiguity and determine the LOS Doppler meteor velocity. This also is an improvement over Janches et al. (2014a). Because the remote stations each have only a single receiving antenna, the derived Doppler velocities at these sites are the speeds along the bisector direction defined by the angle at the meteor between SAAMER-C and the remote site (Janches et al. 2002), while the Doppler velocity derived at SAAMER-C represents the LOS velocity, given that that the transmitter and receiving arrays are colocated for all practical purposes (i.e., the distance between transmitting and receiving antenna is an order of magnitude smaller than the distance from the radar to the meteor). Dividing the Doppler velocities by the cosine of the angle between the derived meteor trajectory and the bisector vector, in the case for the remote sites, or the radial velocity vector, in the case for SAAMER-C, gives the estimated total velocity. In theory, for the case of the remote sites, the angles need to be calculated separately for each pulse using the derived meteor position (see Figure 10). However, since the radar stations are relatively close to one another as compared to the distance from any of the stations to the meteor, these angles are only a few degrees and exhibit very small variations between consecutive pulses.

The advantage of obtaining velocities from the Doppler signature of the return signal is that we can determine instantaneous velocities for each IPP, as opposed to an average meteoroid velocity obtained from the slope of the distance traveled as a function of time such as those displayed in Figure 9. Absolute velocity as a function of IPP measured at each radar site is displayed in Figure 11 for the same event displayed in Figure 9. For this particular head echo event, the estimated velocities from all four radar receiving stations agree
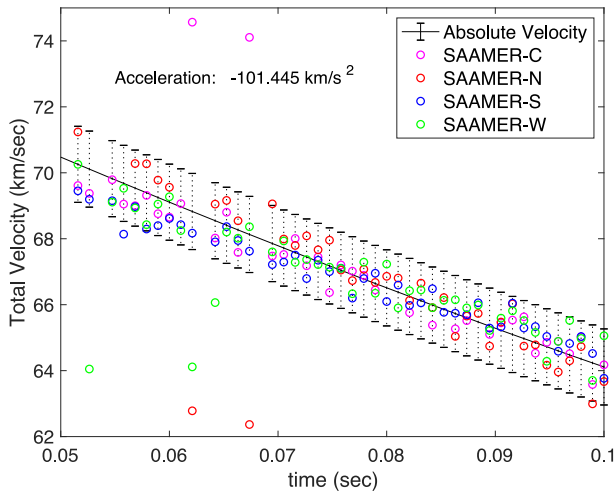
Figure 11. Doppler velocity estimates from each receiver divided by the cosine of the angle to the derived meteor trajectory. The black profile and error bars represent the total absolute velocity derived from the interferometric solution at SAAMER-C using a least-squares fit. Same event as in Figure 6.

to within $1.2\,\mathrm{km\,s^{-1}}$. The black-colored profile represents the total absolute velocity derived from the interferometric solution at SAAMER-C. The uncertainties displayed in Figure 11 were calculated from a least-squares fit of the black-colored profile. We find that uncertainties are $\sim 1\,\mathrm{km\,s^{-1}}$ when velocities are calculated from the position vector, while velocities estimated from Doppler velocity measurements have an uncertainty from 0.3 to $2.7\,\mathrm{km\,s^{-1}}$ (not shown). Because of the ability to measure instantaneous velocity using Doppler signature, it is possible to estimate also the absolute acceleration, which for the case of the event displayed in Figure 11 resulted in $\sim -101.5\,\mathrm{km\,s^{-2}}$. It is important to note that this deceleration is calculated following the formalism described in Chau & Woodman (2004), which corrects for biases based on the meteor's trajectory relative to the receiver's location. We use Equation (4) from Chau & Woodman (2004) to calculate this value, given by

$$|a| \approx a_r + \frac{|v|\Delta\alpha\cos\theta}{\Delta t}, \qquad (11)$$

where $|a|$ is the absolute acceleration, a_r is the radial acceleration (determined from the slope in Figure 11, for example), $|v|$ is the absolute velocity, $\Delta\alpha$ is the angular coverage, and θ is the elevation angle of the meteor trajectory. All of these parameters can be derived from the interferometric solution.

In the next section, we present a summary of results obtained throughout the observing campaign.

4. Results and Discussion

As mentioned earlier, the observations reported here were specifically planned to take place during the anticipated peak of activity of the 2019 β-Taurid meteor shower, when an outburst was expected (Clark et al. 2019). It is important to note that the β-Taurid radiant has a decl. equal to $\delta = +20.1°$. Given SAAMER's latitude of $\sim -53.8°$, the shower radiant reaches a maximum altitude of $16°$ above horizon, which is not optimal for these observations, and thus we did not expect to detect large number of events. Figure 12 shows the head echo rate from SAAMER during the observation period covering June

26–30. Over the course of 5 days, SAAMER detected 71 head echo events averaging between 1.0 and 1.5 head echoes per hour, similar to the detection rate reported by Janches et al. (2014a). During the first and last day of the campaign, SAAMER did not transmit in head echo mode (i.e., eight transmitting antennas in phase) for the full day; however, during the middle 3 days, it detected ~ 20 head echoes per day. These low detection rates, which most likely correspond to larger objects, are expected given the lower sensitivity of SAAMER compared to the HPLA radars (Janches et al. 2014a), indicating also that we did not observe a sudden increase due to the outburst. While the 71 events were also observed at the remote receiving stations, only 12 of the events had S/N sufficiently strong to perform our remote-site velocity determination methods. In a majority of cases, the events exhibited weak to moderate S/N and could only be analyzed with SAAMER-C data, by using the interferometry-only methodology, as they were too faint at the single antenna remote sites to process the raw data and extract reliable ranges.

The bottom panel of Figure 12 displays the number of head echoes detected per hour throughout the entire campaign period. Observations were ongoing throughout the entire day; however, most of the events occurred between local midnight and 2:00 p.m. A clear decrease in the number of detection after 2:00 p.m. is seen, which is consistent with the diurnal behavior of meteor head echoes from the sporadic background observed by HPLA radars (Janches et al. 2006, 2014a; Fentzke & Janches 2008; Sparks & Janches 2009).

The initial height distribution for each observed head echo event, i.e., the altitude at which the first pulse is recorded, is shown in Figure 13, where the blue bars represent events where the data were only processed for SAAMER-C, while the orange bars represent events where the meteor S/N was sufficiently strong at the remote sites, allowing all three analysis methodologies to be performed. This same color convention is used for the remaining plots in this section. We see that almost half of the events peak between 105 and 115 km, with an unusual spike around 95 km. There are also five events whose initial altitudes are greater than 125 km. Although recent studies with the JRO in Peru reported by Gao & Mathews (2015) measured head echoes up to 180 km of altitude, in general head echo detections above ~ 110 km are higher-than-average measured altitude distributions by HPLA radars (Schult et al. 2017; Swarnalingam et al. 2019). Such high-altitude meteor head echoes might be explainable by sputtering of electrons from comparably large meteors as indicated by the Meteor Ablation Model for Radio Optical surveys (MARS; Schult et al. 2020). In order to form a head echo, significant ablation and ionization are required, in particular for radars like SAAMER, whose sensitivity is low compared to HPLA radars (Janches et al. 2008, 2014a). For this to happen, the atmosphere must be dense enough with respect to the meteoroid size, which is not the case above 110 km, unless the meteoroids are large (Janches et al. 2009, 2014b, 2015b, 2017; Schult et al. 2015; Marshall et al. 2017). In fact, as discussed in detail in the introduction of Gao & Mathews (2015), most of the previous studies reporting high-altitude events involved optical detection, which in general observed larger particles (Brown et al. 2017). This is in agreement with the argument that SAAMER-detected head echoes are produced by larger particles than most of the HPLA observations as argued by Janches et al. (2014a)
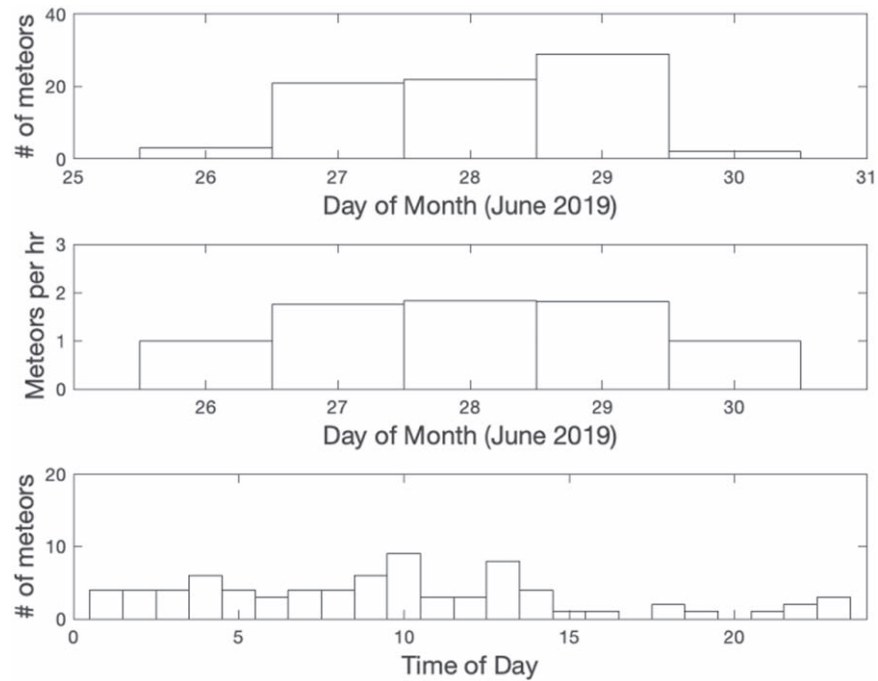
Figure 12. Top: number of meteors detected per day. Middle: average number of meteors detected per hours. Bottom: number of meteors observed at each hour over the entire period of observation.
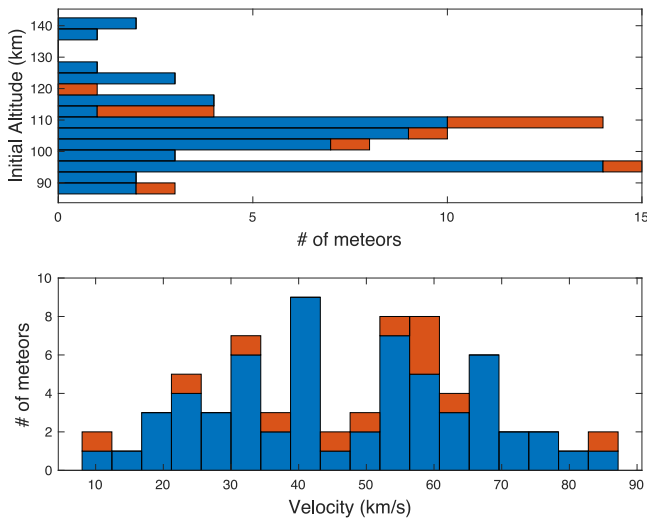

Figure 13. Top: observed initial altitude distribution. Bottom: observed total velocity distribution. Blue bars represent events only processed for SAAMER-C. Orange bars represent multistatic events.
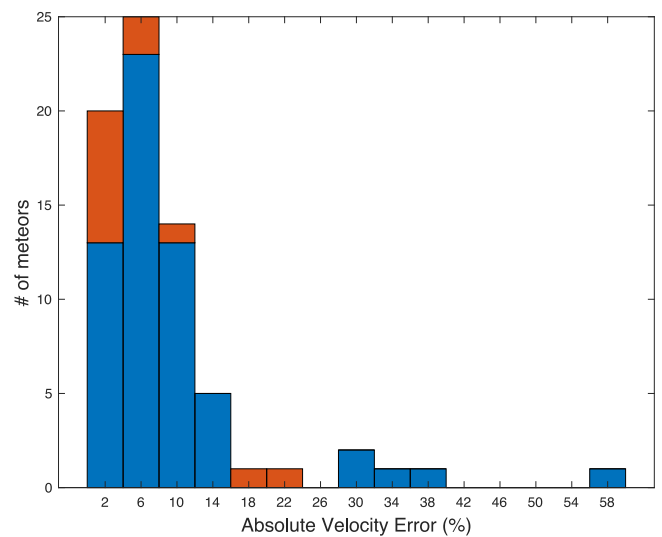

Figure 14. Distribution of velocity error estimates. Blue bars represent events only processed for SAAMER-C. Orange bars represent multistatic events.

and estimated by the optical–radar comparisons reported by Michell et al. (2015).

The bottom panel of Figure 13 displays the total velocity distribution for the 71 events detected during this observing campaign. Even though the number statistics are low, the results suggest the presence of the typical bimodal distribution, showing the indication of two populations with speeds below and above $40 \, \mathrm{km \, s^{-1}}$. The uncertainties of these velocities are determined by propagating the errors of the best-fit line for each x, y, and z velocity component (Figure 9). For a large majority of events, the velocity uncertainty was less than 20% as shown in Figure 14, while only a few cases exceeded this value. These errors are comparable to those obtained by Janches et al. (2014a). However,

for the majority of the events that were detected at all radar sites, and thus the velocity could be determined using all three different methodologies (orange bars), the velocity errors are lower by a factor of five ($\leqslant 4\%$) than those obtained in the past. This is not surprising, as these events had large S/Ns and lead to more accurate estimations of position and velocity. Overall, the median uncertainty in this distribution result is 6%, compared to ~10% that was reported by Janches et al. (2014a). The lower uncertainty is a result of using a 7 bit Barker code compared to the monopulse code used by Janches et al. (2014a) and the inclusion of remote sites to more accurately derive the meteor position vector.

Distributions of horizontal, vertical, and absolute distances through which the head echoes were observed are presented in
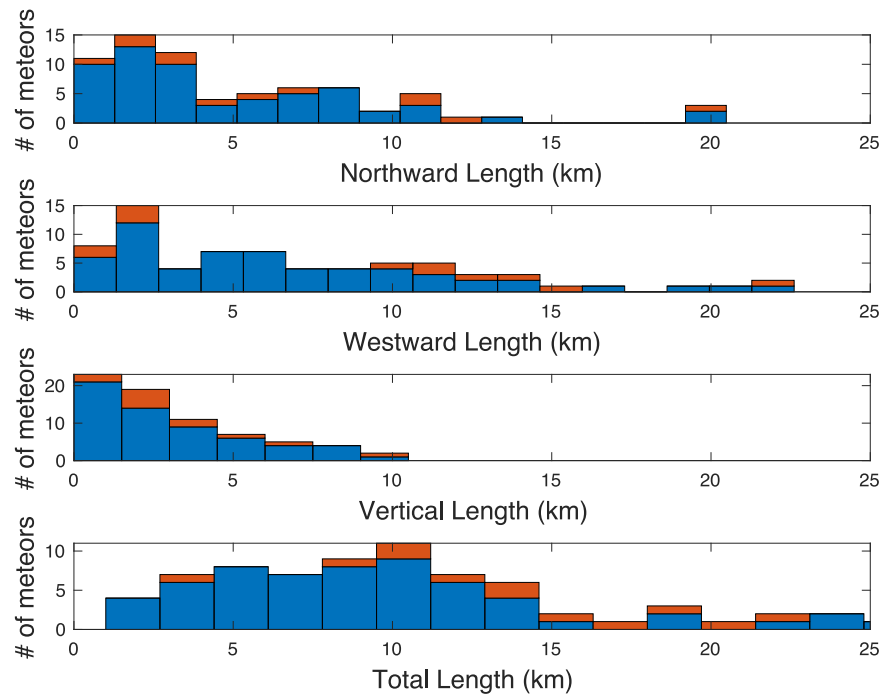
Figure 15. The top three panels display the distribution of the spatial coverage of the head echo events in the three directions. The fourth panel displays the distribution of the absolute observed displacement. Blue bars represent events only processed for SAAMER-C. Orange bars represent multistatic events.

Figure 15. The majority of observed meteors traveled between 2 and 6 km in the vertical direction. The majority of events that were detected by the remote sites (orange bars) had absolute distances (bottom panel) larger than 10 km. The relatively long-lived characteristics of these events are an additional indication that these head echoes are produced by relatively larger particles than those detected by more sensitive HPLA radars (Janches et al. 2014a).

Finally, Figure 16 displays the distribution of meteor entry angles derived from the interferometric solution. The entry angle is defined here as the zenith angle of the meteoroid trajectory, where $0°$ corresponds to a path parallel to the local vertical axis. The estimated entry angles indicate that almost all of the detected head echoes were produced by meteoroids entering the atmosphere at an angle smaller than $40°$ with respect to the local zenith, while almost no meteors entered the atmosphere at angles greater than $45°$. These results agree with previous modeling studies reported by Janches et al. (2006), Fentzke & Janches (2008), and Fentzke et al. (2009), as well as a previous head echo observation campaign using SAAMER (Janches et al. 2004, 2014a).

4.1. Optical Observations

Simultaneous optical observations were made, which can allow for further insight into meteoroid ablation and to constrain key parameters such as the meteoroid ionization coefficient and luminous efficiencies (Weryk & Brown 2013; Brown et al. 2017). The weather conditions during the observing dates, however, were not favorable, and so we only utilize these observations in this study as an additional validation to gain confidence in our velocity determination methodology. Only two head echo events that were simultaneously detected by SAAMER and the video cameras were identified. Figure 17 compares their trajectory solutions, and Figure 18 displays the optical images for the two events. The left and right panels of Figure 17 show a strong and weak event, respectively, as well as their associated velocities. In particular, the
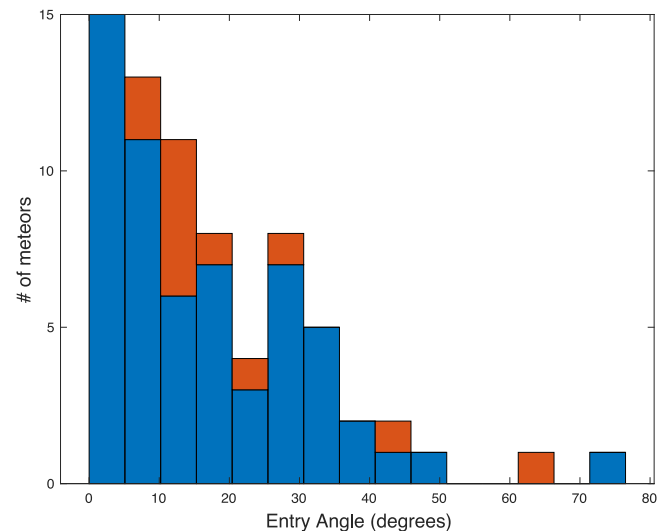

Figure 16. Distribution of calculated entry angle measured from the local zenith. Blue bars represent events only processed for SAAMER-C. Orange bars represent multistatic events.

event displayed in the left panel is the same event presented in Figures 6, 9, and 11. Both the northward and westward radar-derived directions agree with the optical data. The vertical, or altitude, direction overlaps quite well for the right panel,; however, there is a clear mismatch of 5 km between the radar and optical data in the left panel. The source of this discrepancy is due to the low convergence angle of the event on the left panels of Figure 17. For a given optical camera, a plane containing the camera station and the optical detected trail can be defined. The convergence angle is defined as the angle between the planes formed by the various cameras used for the particular detection. The smaller this angle is, the larger the uncertainty in the estimated altitude of the event. The head echo in the left panel had
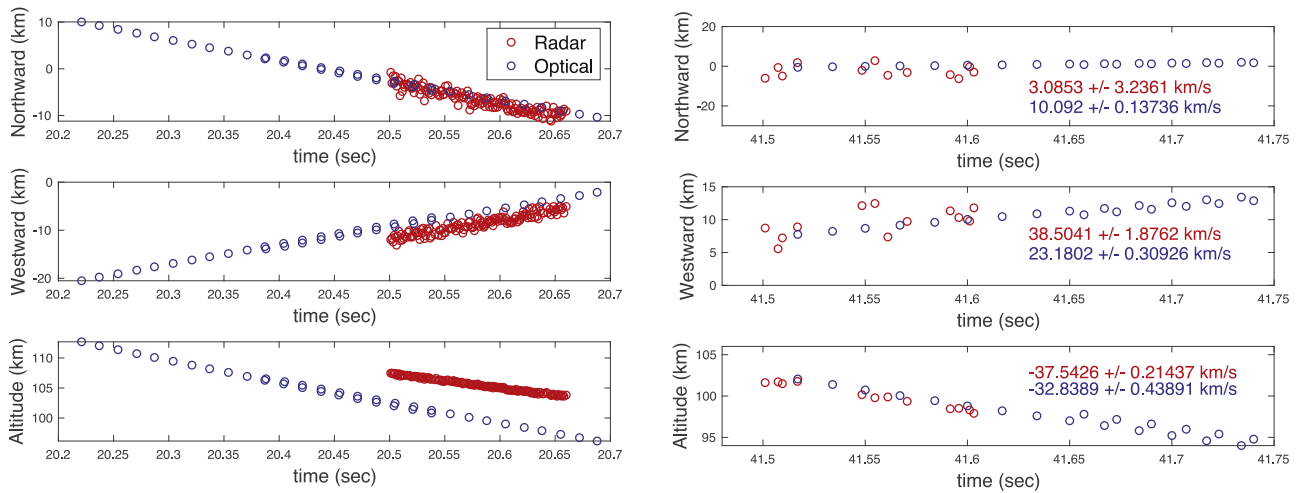
Figure 17. Left and right panels show derived position trajectories using optical (blue) and radar (red) data for two observed events, respectively. Mean velocities are calculated by performing a linear fit to the derived position as a function of time.
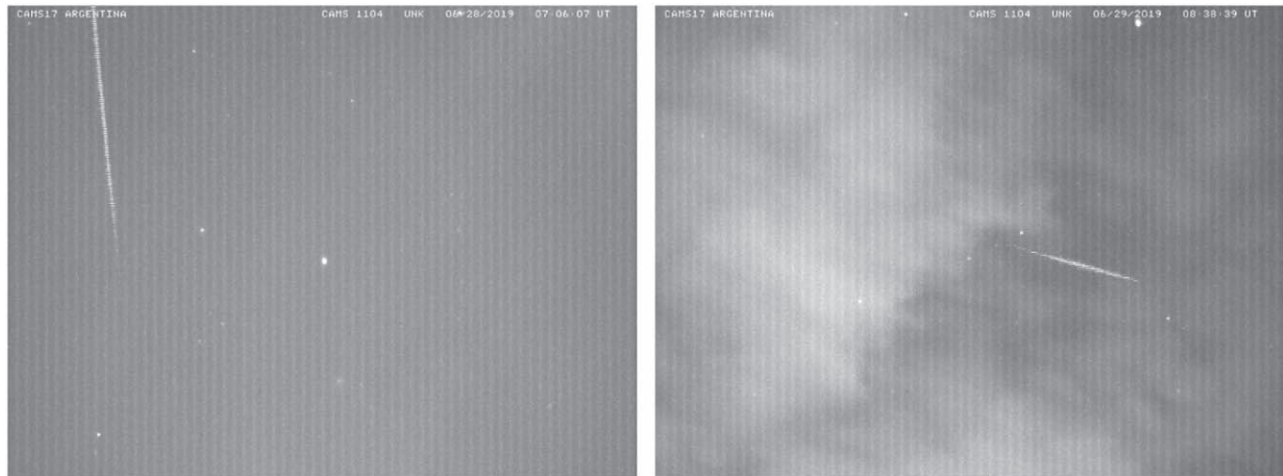

Figure 18. Optical image data for the two events simultaneously observed by SAAMER and ONAS-DREAM. Left and right panels corresponds to the same events as the left and right panels in Figure 17.

Table 2
Derived Absolute Velocities Using Radar and Optical Data for a Single Meteor Head Echo

	Interferometry	Prolate Sphere	3-Sphere	Doppler	Optical
Absolute Velocity (km s^{-1})	67.03	82.48	71.51	67.21	68.04
Velocity Error (km s^{-1})	1.30	6.94	6.11	3.12	0.42

a convergence angle of 3.2°, while the event in the right panel was 32.3°. Overall, the two events shown in Figure 17 demonstrate that agreement is found in the radar and optical observations, suggesting that these are simultaneous radar and optical detections of the same events.

There was only one simultaneous head echo-video event that was observed by all four SAAMER sites. The derived position vectors of this event are displayed in Figure 9 and the left panel of Figure 17. A comparison of the absolute velocities and their associated uncertainties for each method used to derive its characteristics are listed in Table 2. The agreement between the results determined with the interferometry methodology, the optical observations, and the Doppler velocities is excellent. Good agreement is also found with the 3-sphere methodology. Only the method that utilizes prolate spheroids to determine the position vector differed by more than 10 km s^{-1}; however, it

was also the method that produced the largest error in velocity. Even though the altitude vector for the optical data shows a shift in the true trajectory due to the poor convergence angle, this did not appear to influence the absolute velocity.

4.2. Orbits

The velocity of each meteor was fit, neglecting deceleration, to the pulse-by-pulse Cartesian position coordinates of each event. The local radiant was converted into equatorial coordinates and, together with the speed, transformed into heliocentric Keplerian orbital elements, with the position of Earth given by the JPL DE-430 planetary ephemeris (Folkner et al. 2014). As these are osculating elements at the epoch of observation, no perturbations are applied.

Table 3
β-Taurid Orbits, Where the Epoch Is the Observed UTC Time on 2019 June 29

Element	Brown (2008)	Orbit 1	Orbit 2
a	1.66 au	3.239 au	1.800 au
e	0.8042	0.867	0.765
i	3.6°	4.2°	1.7°
ω	238.3°	256.25°	249.73°
Ω	277.0°	277.07°	277.08°
q	0.325 au	0.432 au	0.423 au
M	…	7.3°	19.3°
Epoch	…	18:10:08	18:11:02
D'	…		

Note. The reference shower orbit is from Brown et al. (2008), used to compute the D' criterion values.

The Drummond D' criterion (Drummond 1981) was used to identify potential shower members, by comparing the orbital elements to those available in the literature, or elsewhere,[8] including the comet catalog from the Minor Planet Center. We found two likely β-Taurid shower members, showing that the stream was active (Clark et al. 2019), and at the time of the preparation of this work, we are not aware of any other studies having detected this shower. We list these two orbits, along with the stream orbit from Brown et al. (2008), in Table 3.

While the uncertainty propagation in the fitted trajectories is straightforward to compute, a proper error analysis requires a detailed investigation into deceleration correction, which is beyond the scope of this work. As we simply want to search our orbit list for possible shower members, we defer this analysis to future work on individual meteor-parent searches.

We note that, like many radar meteor studies, a fraction of our computed orbits are hyperbolic, but we do not believe this to be their true nature. As head echoes are observed over an even shorter time span than the typical time-of-flight trail echo method used by SAAMER-OS and others, the expected uncertainties will be even larger.

5. Conclusions

Recently, non-HPLA radars such as SAAMER have developed the capability of detecting meteor head echoes (Janches et al. 2014a; Schult et al. 2015). In this work, we improve the meteor head echo observing technique to enhance range resolution by modifying the transmitting mode and using a 7 bit Barker code. We performed radar observations during a period of expected high activity of the β-Taurid meteor shower, between 2019 June 26 and 30. Using the full capabilities of the SAAMER Orbital System, we derived meteor properties from head echo radar observations using two techniques: (1) interferometry by leveraging the five-antenna arrangement at SAAMER-C, and (2) target localization using simultaneous observations from at least three radar stations separated by at least 8 km.

During the meteor campaign, SAAMER observed 71 head echo events (roughly 1.5 events per hour) capable of interferometric analysis. A majority of these events had initial altitudes from 100 to 110 km, while three events were observed above 135 km. Although higher than average, these high-altitude events suggest that SAAMER-detected head echoes are produced by

larger particles than most of the HPLA observations. A bimodal velocity distribution was observed showing two populations with speeds below and above 40 km s^{-1}. Twelve of the events were simultaneously observed with high S/N at the three remote sites for which target localization methods were used to derive meteor characteristics. The trajectories and velocities derived from the data of these strong events produced the lowest uncertainty, compared to events only detected at SAAMER-C. Further, deceleration estimations of a few meteors could be calculated for the strongest events.

Video cameras were also deployed to observe the meteor shower in tandem with SAAMER. Due to poor weather, only two events were simultaneously detected with optical and radar instruments. The absolute velocity derived from the optical images, however, was in very good agreement with interferometry and Doppler methods using radar data to within 1–2 km s^{-1}, while the target localization approach derived slightly higher velocities, albeit still within uncertainties.

Heliocentric meteoroid orbits were computed from the trajectory solutions and compared to the expected β-Taurid parent orbit. While many of our orbital solutions are hyperbolic, this is likely not their true nature, but rather due to the large uncertainty associated with the extremely short time period over which a head echo occurs. We identified two possible β-Taurid meteoroids.

This work demonstrates a powerful methodology developed using SAAMER-OS to perform future focus studies with targeted and better observational-suited meteor showers and obtain critical measure to understand the physical properties of their meteoroids.

6. Software and Third-party Data Repository Citations

The results of calculations presented in this study are available on the Open Science Framework website: doi:10. 17605/OSF.IO/5XEJ8.

ORCID iDs

Peter A. Panka ● https://orcid.org/0000-0001-9801-8249
Robert J. Weryk ● https://orcid.org/0000-0002-0439-9341
Juan S. Bruzzone ● https://orcid.org/0000-0002-2731-0397
Diego Janches ● https://orcid.org/0000-0001-8615-5166
Gunter Stober ● https://orcid.org/0000-0002-7909-6345
Jose Luis Hormaechea ● https://orcid.org/0000-0003-4533-3282

---
[8]   https://www.ta3.sk/IAUC22DB/MDC2007/

References

Baggaley, W. 2002, in Meteors in the Earth's, ed. E. Murad & I. Williams (Cambridge: Cambridge Univ. Press), 123
Brown, P., Stober, G., Schult, C., et al. 2017, P&SS, 141, 25
Brown, P., Weryk, R. J., Wong, D. K., & Jones, J. 2008, Icar, 195, 317
Chau, J. L., & Woodman, R. 2004, ACP, 3, 6063

Clark, D. L., Wiegert, P., & Brown, P. G. 2019, MNRAS Letters, 487, L35
Close, S., Hunt, S., Minardi, M., & McKeen, F. 2000, RaSc, 35, 1233
Close, S., Oppenheim, M., Durand, D., & Dyrud, L. 2005, JGRA, 110, 9308
Close, S., Oppenheim, M., Hunt, S., & Dyrud, L. 2002, JGRA, 107, 1295
Close, S., Volz, R., Loveland, R., et al. 2012, Icar, 221, 300
Drummond, J. D. 1981, Icar, 45, 545
Dyrud, L. P., & Janches, D. 2008, JASTP, 70, 1621
Fentzke, J. T., & Janches, D. 2008, JGRA, 113, A03304
Fentzke, J. T., Janches, D., & Sparks, J. J. 2009, JASTP, 71, 653
Folkner, W. M., Williams, J. G., Boggs, D. H., Park, R. S., & Kuchynka, P. 2014, IPNPR, 196, 1, https://naif.jpl.nasa.gov/pub/naif/generic_kernels/spk/planets/de430_and_de431.pdf
Gao, B., & Mathews, J. D. 2015, MNRAS, 446, 3404
Gural, P. S. 1995, JIMO, 23, 228
Gural, P. S. 1997, JIMO, 25, 136
Gural, P. S. 2012, M&PS, 47, 1405
Hagen, J. B., & Farley, D. T. 1973, RaSc, 8, 775
Hocking, W. K., Fuller, B., & Vandepeer, B. 2001, JASTP, 63, 155
Hocking, W. K., Thayaparan, T., & Jones, J. 1997, GeoRL, 24, 2977
Jacchia, L. G., & Whipple, F. L. 1961, SCoA, 4, 97
Janches, D., Bruzzone, J. S., Weryk, R. J., et al. 2020, ApJL, 895, L25
Janches, D., Close, S., & Fentzke, J. T. 2008, Icar, 193, 105
Janches, D., Close, S., Hormaechea, J. L., et al. 2015a, ApJ, 809, 36
Janches, D., Dyrud, L. P., Broadley, S. L., & Plane, J. M. C. 2009, GeoRL, 36, 6101
Janches, D., Heinselman, C. J., Chau, J. L., Chandran, A., & Woodman, R. 2006, JGRA, 111, A07317
Janches, D., Hocking, W., Pifko, S., et al. 2014a, JGRA, 119, 2269
Janches, D., Mathews, J., Meisel, D., Getman, V., & Zhou, Q. 2000a, Icar, 143, 347
Janches, D., Mathews, J., Meisel, D., & Zhou, Q. 2000b, Icar, 145, 53
Janches, D., Nolan, M., & Sulzer, M. 2004, ACP, 4, 621
Janches, D., Pellinen-Wannberg, A., Wannberg, G., et al. 2002, JGR, 107, 1389
Janches, D., Plane, J. M. C., Nesvorný, D., et al. 2014b, ApJ, 796, 41
Janches, D., Swarnalingam, N., Carrillo-Sanchez, J., et al. 2017, ApJ, 843, 11
Janches, D., Swarnalingam, N., Plane, J. M. C., et al. 2015b, ApJ, 807, 13
Jenniskens, P., Gural, P. S., Dynneson, L., et al. 2011, Icar, 216, 40

Jones, J., Webster, A. R., & Hocking, W. K. 1998, RaSc, 33, 55
Kero, J., Campbell-Brown, M. D., Stober, G., et al. 2019, in Meteoroids: Sources of Meteors on Earth and Beyond, ed. G. O. Ryabova, D. J. Asher, & M. D. Campbell-Brown (Cambridge: Cambridge Univ. Press), 65
Kero, J., Szasz, C., Nakamura, T., et al. 2011, MNRAS, 416, 2550
Kero, J., Szasz, C., Nakamura, T., et al. 2012, AnGeo, 30, 639
Kero, J., Szasz, C., Pellinen-Wannberg, A., et al. 2008a, AnGeo, 26, 2217
Kero, J., Szasz, C., Wannberg, G., Pellinen-Wannberg, A., & Westman, A. 2008b, GeoRL, 35, L07101
Lau, E. M., Avery, S. K., Avery, J. P., et al. 2006, RaSc, 41, 4007
Marshall, R. A., Brown, P., & Close, S. 2017, P&SS, in press
Mathews, J. D. 1976, JGR, 81, 4671
Mathews, J. D., Janches, D., Meisel, D., & Zhou, Q. 2001, GeoRL, 28, 1929
Mazur, M., Pokorný, P., Brown, P., et al. 2020, RaSc, 55, e06987
McKinley, D. W. R. 1961, Meteor Science and Engineering (New York: McGraw-Hill)
Michell, R. G., Janches, D., Samara, M., et al. 2015, P&SS, in press
Pifko, S., Janches, D., Close, S., et al. 2013, Icar, 223, 444
Schult, C., Kero, J., Stober, G., & Brown, P. 2021, Icar, 355, 114137
Schult, C., Stober, G., Brown, P., Pokorný, P., & Campbell-Brown, M. 2020, Icar, 340, 113444
Schult, C., Stober, G., Chau, J. L., & Latteck, R. 2013, AnGeo, 31, 1843
Schult, C., Stober, G., Janches, D., & Chau, J. L. 2017, Icar, 297, 1
Schult, C., Stober, G., Keuer, D., & Singer, W. 2015, MNRAS, 450, 1460
Sparks, J. J., & Janches, D. 2009, GeoRL, 36, 12105
Sparks, J. J., Janches, D., Nicolls, M. J., & Heinselman, C. 2010, JASTP, 72, 1221
Sparks, J. J., Janches, D., Nicolls, M. J., & Heinselman, C. J. 2009, JASTP, 71, 644
Stober, G., Schult, C., Baumann, C., Latteck, R., & Rapp, M. 2013, AnGeo, 31, 473
Swarnalingam, N., Janches, D., Carrillo-Sanchez, J. D., et al. 2019, AJ, 157, 179
Vondrak, T., Plane, J. M. C., Broadley, S., & Janches, D. 2008, ACP, 8, 7015
Weryk, R. J., & Brown, P. G. 2013, P&SS, 81, 32
Whipple, F. L., & Jacchia, L. G. 1957, SCoA, 1, 183